Tradeoffs in anti-scatter grid for energy-resolved photon counting detector

Yannan Jin, Geng Fu, Xue Rui and Peter M. Edic
GE Global Research, Niskayuna, NY

Abstract— **The goal of this study is to investigate the tradeoff in the design of anti-scatter grid for a photon-counting detector. The anti-scatter grid can block the primary beam at the boundary of each detector pixel, which reduces the charge sharing. On the other hand, thick anti-scatter grids also reduce the detector fill factor and thus reduce dose efficiency. To quantitatively evaluate the performance of spectral imaging, we use both CRLB-based metrics from analytic calculation and CNR-based metrics from projection-based simulation. The results indicate that the use of anti-scatter grid can reduce the charge sharing, but its dose penalty in geometric efficiency outweighs the dose benefit in spectral separation. Therefore, thinner anti-scatter grid plates are preferred for photon-counting detectors in both single-energy and spectral imaging.**

Index Terms— **photon-counting detector, anti-scatter grid, material decomposition, Cramér-Rao Lower Bound**

I. INTRODUCTION

X-RAY CT with an energy-resolved photon-counting detector (PCD) has great potential in medical imaging [1]. Unlike conventional scintillator-based, energy-integrating detectors, most PCDs use semiconductor materials such as cadmium telluride (CdTe) or cadmium zinc telluride (CZT) to convert incident X-ray photons directly into electrical signals. The energy of individual incident photons, inferred from the detected signal, provides an extra dimension of information that can be used to distinguish materials [2]. Besides the spectral information, the potential benefits of PCDs also include the high spatial resolution and the superior noise performance at low dose [3,4].

However, as an emerging technology, PCDs also face technical challenges, such as the pile-up effect that distorts the detected energy spectrum and decreases quantum efficiency at high photon flux [5], and charge sharing and K-fluorescence that degrades the energy resolution at small detector pixel size. To mitigate the impact of these effects, tradeoffs need to be made in detector design. For example, Hsieh and Pelc studied the pixel size tradeoffs for CdTe photon-counting detectors based on the Cramér-Rao Lower Bound (CRLB) of variance

[6]. We also investigated the selection of pixel size, material thickness, and electronic noise for a CZT-based photon-counting detector [7].

The goal of this study is to investigate the tradeoff in the design of an anti-scatter grid for a photon-counting detector. The anti-scatter grids not only absorb the scattered radiation emitted from body tissue before reaching the detector, but also block the primary beam at the boundary of each detector pixel, which significantly reduces charge sharing. On the other hand, thick anti-scatter grids also reduce the detector fill factor and thus reduce dose efficiency. In this study, we compare the performance of spectral CT with different designs of anti-scatter grids.

Two types metrics are used to evaluate the performance of photon-counting detectors: Contrast-to-noise ratio (CNR) based metrics [8,9] and Cramér-Rao Lower Bound (CRLB) based metrics [10-12]. In Section II.C we illustrate the relationship between the two types of metrics. In Section III we compare results based on CRLB and CNR, demonstrating that the two metrics are equivalent to each other.

II. MATERIALS AND METHODS

A. Detector Spectral Response

A Geant4-based Monte Carlo simulation was used to consider the 3D X-ray energy deposition in the sensor. Charge is generated, diffused according to CZT material properties and the electric field within the semiconductor detector, and transported to respective anode/cathode electrodes. Charge induction in a charge-sensitive amplifier was simulated while
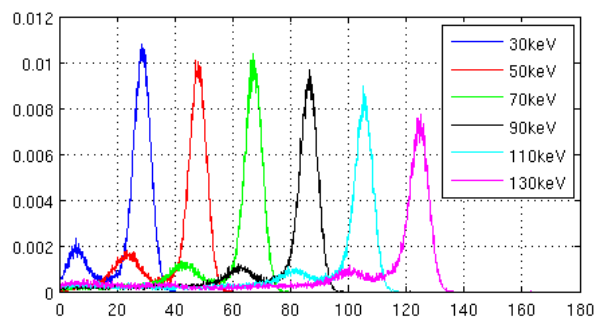
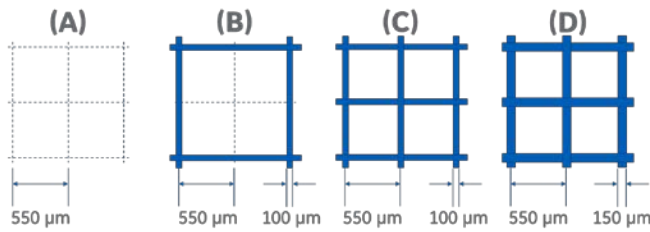Figure 1: Spectral response to monochromatic X-ray inputs at various energies. The results are based on Monte Carlo simulation.

Figure 2: Four detector collimator options - detector pitch at 550 μm. (A) no collimator, (B) collimator at 2x2 pixels with thickness of 100 μm, (C) and (D) collimator at 1x1 pixel with thicknesses of 100 μm and 150 μm, respectively.

considering the 3D weighting potentials for different detector configurations; band-pass filtering (fast shaper) was applied; and electronic noise added to the output signal. Figure 1 shows an example of the generated spectral response functions, when considering mono-energetic X-ray photon input at various energies.

B. Collimator Design

Three collimator design options were studied as illustrated in Figure 2 (B)-(D). The pixel size of 550 μm is selected following the optimization work described in [7]. The collimator designs (C) and (D) assume 2D collimation at each detector pixel with a collimator thickness of 150 μm and 100 μm, respectively. Design (B) assumes that the collimation at every 2x2 pixels with a thickness of 100 μm.

Collimator blades are commonly made of highly-attenuating materials such as tungsten; therefore, collimator designs (C) and (D) have similar performance in rejecting scattered X-rays if the collimator blades all have the same height. However, the design (D) can better reject charge sharing and K- fluorescence more effectively due to increased blade thickness. Design (B) has the lowest performance in rejecting scatter and charge sharing, but the detector pixels have a better fill factor and hence a higher geometric efficiency.

C. Evaluation criteria

To quantitatively evaluate the tradeoffs in overall dose efficiency with the different collimator designs, an evaluation metric needs to be defined.

In this paper, we focus on the spectral imaging performance which reflects the capability to differentiate different materials. As shown in Figure 3, the area of the noise cloud in the basis material coordinates after projection-based material decomposition (MD) is a good indicator of material separability. Thus, the first metric is defined as the area of the elliptical noise cloud after MD with two basis materials multiplied by dose (variance-dose product):

$$VDP_1 = \pi \sigma_{opt-mono} \cdot \sigma_{ortho} \cdot D \qquad (1)$$

where $\sigma_{opt\ mono}$ and σ_{ortho} are the standard deviation along and orthogonal to the direction of the optimal monochromatic energy (maximum CNR), respectively. D represents the total dose absorbed by the object which is proportional to tube current (mA), while the product of $\sigma_{opt-mono}$ and σ_{ortho} is inversely proportional to the mA. Thus, the impact of tube current gets cancelled out.
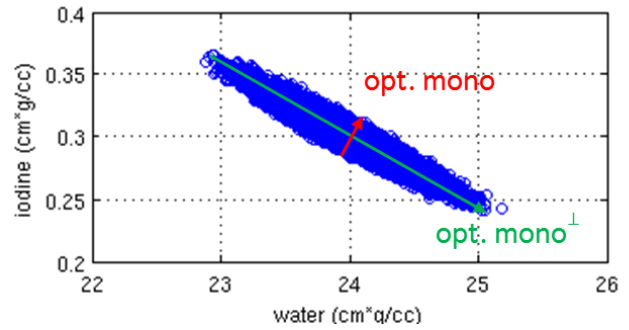

Figure 3: Noise cloud of basis materials after projection-based material decomposition. The direction along and orthogonal to the optimal monochromatic energy corresponds to the direction of two eigenvectors of the inversion of the Fisher Information Matrix.

The second metric utilizes the Cramér-Rao Lower Bound (CRLB) in previous studies [10-12]. As Rossel and Hermann described in [10], for X-ray CT systems with PCDs, the Fisher Information Matrix can be written as

$$\mathcal{F}_{\alpha\beta} = \sum_{i=1}^{N_C} \frac{1}{v_i} \frac{\partial v_i}{\partial A_\alpha} \frac{\partial v_i}{\partial A_\beta} \qquad (2)$$

where v_i is the mean value of the number of photons detected in the ith energy bin; A_α and A_β are the line integral of the basis material density distribution (i.e. the area densities of basis material α and β); N_C is the total number of energy bins of the photon-counting detector.

According to Cramér-Rao inequality [10], the lower bounds of the variance of basis materials are the inverse of the Fisher Information Matrix (i.e. $\sigma_{A_\alpha}^2 \geq \mathcal{F}_{\alpha\alpha}^{-1}$). Moreover, the eigenvalues of the inverse of the Fisher Information Matrix represent the lower bounds of the variance along the axes of the noise cloud ellipse (2-basis material) or ellipsoid (3-basis material), as illustrate in Figure 3. Thus, the second metric is CLRB-based and can be written as

$$VDP_2 = \pi \prod_{\alpha=1}^{M} \sqrt[M]{\lambda_\alpha(\mathcal{F}^{-1})} \cdot D \qquad (3)$$

where M is the number of basis materials; $\lambda_\alpha(\mathcal{F}^{-1})$ represents the αth eigenvector of the matrix $\mathcal{F}^{-1}$. The use of
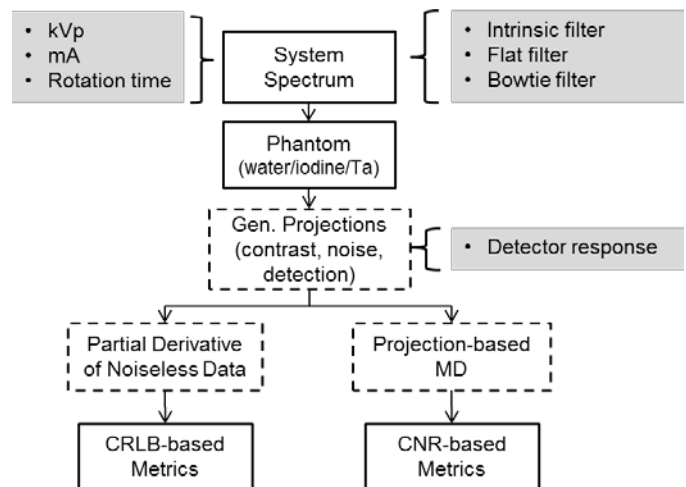

Figure 4: Flowchart for projection data generation, material decomposition, and the generation of CRLB-based metrics and CNR-based metrics

the Mth root and total dose D aims at cancelling the impact of tube current. Thus, the decrease in both evaluation metrics shown in (1) and (3) can be directly interpreted as dose reduction.

D. Experimental Setup

The experiment flowchart is shown in Figure 4. The first metric, as defined in equation (1), was generated by simulating a huge number of projection rays (about 1 million), performing the projection-based MD [13], and calculating the statistics from the simulated data. The second metric in equation (3) was generated based on analytic calculation of the CRLB.

In this study, we simulated a clinical CT scanner equipped with an energy-discriminating, photon-counting detector with up to eight energy bins. A 24-cm water phantom was used to emulate typical patient attenuation. To simulate the contrast agent, we inserted a 3-cm thickness of 10 mg/cc iodine. For K-edge imaging, we also inserted a 3-cm thickness of 10 mg/cc tantalum. The spectrum at 140 kV was produced by the XSPECT package (v3.5), and then filtered with the nominal intrinsic filtration of a typical X-ray tube.

The detector spectral responses of different collimator designs were generated as described in Section II.A. We neglected the complications of the pile-up effect, assuming the photon flux arriving at the detector was low. When the number of energy bins is below three, we calculated the metrics for all energy thresholds and choose the optimal setting; otherwise, we set the energy thresholds by balancing the photon counts in each energy bin.

All cases were normalized to the case when no collimator was used (shown in Figure 2A). Since we used the same spectrum and object, the dose term remained the same and is cancelled in the normalization.

III. RESULTS

The plots of spectral responses corresponding to different detector collimator design options are shown in Figure 5. The response functions exhibit a main photopeak at the incident energy (in this case at 70 keV), which can be well described by a Gaussian distribution [5]. In addition to the main photopeak, the response functions also exhibit a Gaussian-shaped K-escape
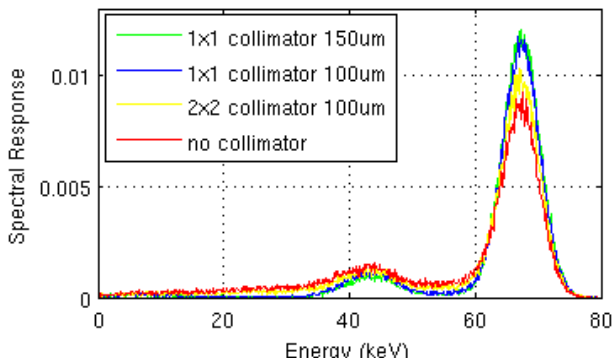

Figure 5: Spectral response function for 70 keV monochromatic incident X-rays when using different collimator design options.
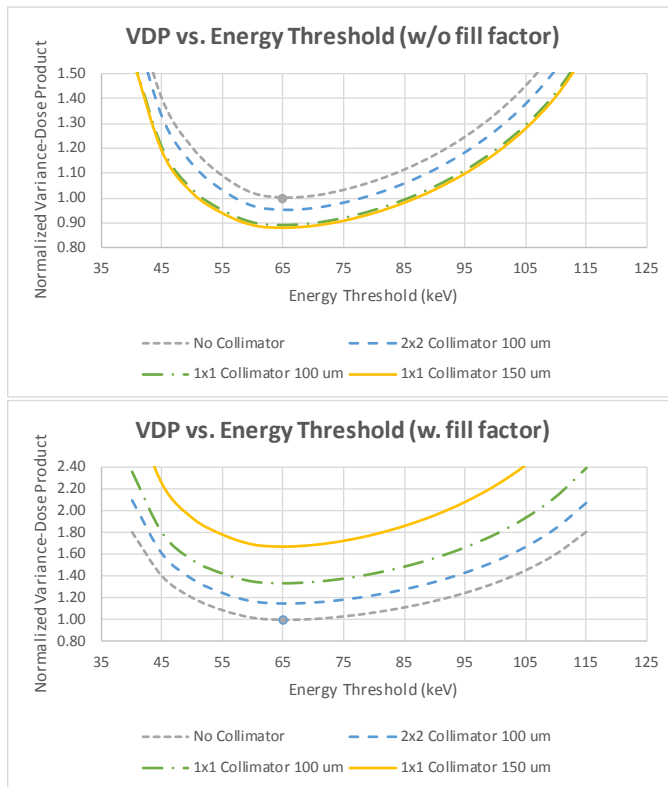

Figure 6: CRLB-based metric (i.e. the size of the noise cloud at given dose) of different collimator design options when the PCD energy threshold is set at different energy levels. The top and bottom plots correspond to results with and without including the effect of the detector fill factor of different collimator design options, respectively.

Table 1 Comparison of results with two metrics
(at optimal energy threshold, with fill factor)

	CRLB-based	CNR-based	Diff (%)
No col.	1.00	1.02	2%
2x2 col. 100 um	1.15	1.18	2%
1x1 col. 100 um	1.33	1.35	1%
1x1 col. 150 um	1.67	1.68	1%

peak caused by K-fluorescence photons emitted from an active pixel and escaping to adjacent pixels, and a relatively constant low-energy tail that is caused by charge sharing. The plots show that the main photopeak when using 1x1 collimators are higher than when not using a collimator, and the charge-sharing tails when using 1x1 collimators are almost eliminated, indicating an effective reduction of charge sharing when the 1x1 collimators are utilized. The K-escape peak, on the other hand, is less sensitive to the changes of collimator.

Figure 6 shows the metric in equation (2) relative to the change of energy threshold in the case of dual-energy imaging for the various collimator configurations. The spectral performance is demonstrated by the plots in the top figure. All results are normalized to the no-collimator case with energy threshold at 65 keV. The 1x1 collimator has the best performance as it corresponds to the minimal noise-dose product. However, when taking the detector fill factor into account, the bottom plots in Figure 6 show that the no-

VDP vs. Energy Bin Number
(3 material, 6 bin, w/o fill factor)

VDP vs. Energy Bin Number
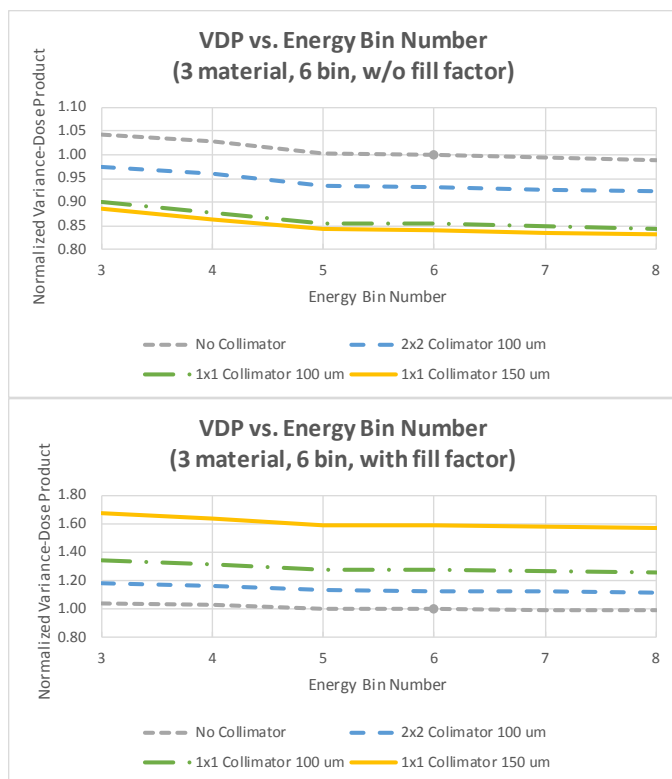### (3 material, 6 bin, with fill factor)

Figure 7: CRLB-based metric with different collimator design options for 3 material MD (water/iodine/tantalum) using up to 8 energy bins. The top and bottom plot correspond to results with and without including the effect of the detector fill factor of different collimator design options, respectively.

collimator case has the best performance, i.e. the dose penalty on the fill factor imposed by the anti-scatter grid outweighs the dose benefit on charge sharing reduction.

Figure 7 shows the CRLB-based results when using multi-energy bins for K-edge imaging. The basis materials were water, iodine and tantalum. The energy bins were properly chosen using the K-edge as an energy threshold. The results were consistent with the two-material case in Figure 6; the dose penalty resulting from the reduced fill factor is more prominent than the dose benefit from reducing charge sharing. As shown in the bottom plot in Figure 7, the no-collimator case has the highest overall dose efficiency when the detector fill factor is incorporated.

Table 1 compares the results for CRLB-based metrics and CNR-based metrics. All results are normalized to the no-collimator case when using the CRLB-based metric. The results using the two different metrics match well, demonstrating the validity of using analytic calculations to derive the size of the noise cloud after MD.

IV. DISCUSSION AND CONCLUSION

The electron clouds generated and diffused in the CZT-based substrate are about 100 μm diameter [1]. Thus, as shown in the spectral response functions in Figure 5, the 1x1 collimator scheme with thickness of both 100 μm and 150 μm can effectively eliminate the low-energy tail caused by charge sharing. The 2x2 collimator can only eliminate about half of the charge sharing; therefore, its spectral response function is

between the energy response function when using a 1x1 collimator and that when using no collimator.

The results of both CRLB-based metric and CNR-based metric indicate that, although the anti-scatter grid can reduce the charge sharing effect and improve spectral separation, the benefit is much lower than the dose penalty caused by the loss of detector geometric efficiency. For single-energy imaging, a thick anti-scatter grid also reduces dose efficiency due to the decrease in fill factor. However, utilizing a detector without a collimator is not an option for state-of-the-art CT scanners due to the degradation of image quality caused by scatter artifacts. Thus, thinner collimator blades are preferred since the septa are made of highly-attenuating materials and most of the scattered photons can be absorbed even with thin blades. The minimum thickness of the collimator blades has certain constraints, such as the manufacturability and the rigidity to G-force at a high rotation speed.

Sophisticated hardware solutions such as coincidence detection circuits are also being investigated [14] to mitigate the charge sharing and K-fluorescence effect. However, this technology is still not practical at high photon flux rate due to the limitations of ASICs [14]. The results of this study indicate that an anti-scatter grid has negative impact on overall dose efficiency relative to the benefit of decreased charge sharing, and only a limited impact on K-fluorescence; therefore, coincidence logic is still a preferred solution to improve the energy resolution and detector efficiency.

In summary, we investigated the spectral performance of energy-resolved photon-counting detectors with different designs of anti-scatter grids. The evaluation metrics of the spectral performance were CRLB-based from analytic calculation and CNR-based from projection-based simulation. The results indicate that the use of anti-scatter grid can reduce charge sharing, but its dose penalty due to geometric efficiency outweighs the dose benefit in spectral energy separation. Therefore, thinner anti-scatter grid plates are preferred for photon-counting detectors in both single-energy and spectral imaging.

REFERENCES

[1] Taguchi, Katsuyuki, and Jan S. Iwanczyk. "Vision 20/20: Single photon counting x-ray detectors in medical imaging." *Medical physics* 40.10 (2013): 100901.

[2] Wang, Xiaolan, et al. "Material separation in x-ray CT with energy resolved photon-counting detectors." *Medical physics* 38.3 (2011): 1534-1546.

[3] Schlomka, JPea, et al. "Experimental feasibility of multi-energy photon-counting K-edge imaging in pre-clinical computed tomography." *Physics in medicine and biology* 53.15 (2008): 4031.

[4] Barber, William C., et al. "Characterization of a novel photon counting detector for clinical CT: count rate, energy resolution, and noise performance." *SPIE Medical Imaging*. International Society for Optics and Photonics, 2009.

[5] Knoll, Glenn F. *Radiation detection and measurement*. John Wiley & Sons, 2010.

[6] Hsieh, Scott S. and Norbert J. Pelc. "Pixel Size Tradeoffs for CdTe Spectral Photon Counting Detectors." *4th International Conference on Image Formation in X-Ray Computed Tomography*. CT-meeting, 2016.

[7] Jin, Yannan, et al. " Design and Optimization of Direct Conversion Photon-Counting Detector for Dual-Energy CT Imaging." *2016 IEEE Nuclear Science Symposium Conference Record (NSS/MIC)*. IEEE, 2016.

[8] Jin, Yannan, et al. "CNR Analysis of Dual Energy Technologies." *3rd International Conference on Image Formation in X-Ray Computed Tomography*. CT-meeting, 2014.

[9] Kappler, S., et al. "Dual-energy performance of dual kVp in comparison to dual-layer and quantum-counting CT system concepts." *SPIE Medical Imaging*. International Society for Optics and Photonics, 2009.

[10] Roessl, E., and C. Herrmann. "Cramér–Rao lower bound of basis image noise in multiple-energy x-ray imaging." *Physics in medicine and biology* 54.5 (2009): 1307.

[11] Wang, Adam S., and Norbert J. Pelc. "Sufficient statistics as a generalization of binning in spectral x-ray imaging." *IEEE transactions on medical imaging* 30.1 (2011): 84-93.

[12] Petschke, Adam, and Yu Zou. "An analytical formula for the covariance matrix of basis material projection estimates in spectral x-ray computed tomography." *Nuclear Science Symposium and Medical Imaging Conference (NSS/MIC), 2015 IEEE*. IEEE, 2015.

[13] R. E. Alvarez and A. Macovski, "Energy-selective reconstructions in X-ray computerised tomography," *Physics in Medicine and Biology*, vol. 21, pp. 733-744, 1976.

[14] Koenig, Thomas, et al. "Charge summing in spectroscopic x-ray detectors with high-Z sensors." *IEEE Transactions on Nuclear Science* 60.6 (2013): 4713-4718.